Template-assisted growth and characterization of ZnO-based nanowire arrays and 3D networks

Application of nanowire networks for photoelectrochemical water splitting

Templat-gestütztes Wachstum und Charakterisierung von ZnO-basierten Nanodrahtarrays und 3D Netzwerken

Zur Erlangung des Grades eines Doktors der Naturwissenschaften (Dr. rer. nat.) genehmigte Dissertation von **M.Sc. Liana Movsesyan** aus Jerewan (Armenien)

Tag der Einreichung: 19.07.2016, Tag der Prüfung: 06.10.2016

1. Gutachten: Prof. Dr. Christina Trautmann
2. Gutachten: Prof. Dr. Wolfram Jaegermann

Material- und Geowissenschaften, D17

Darmstadt - 2017

TECHNISCHE UNIVERSITÄT DARMSTADT

MATERIAL-WISSENSCHAFT

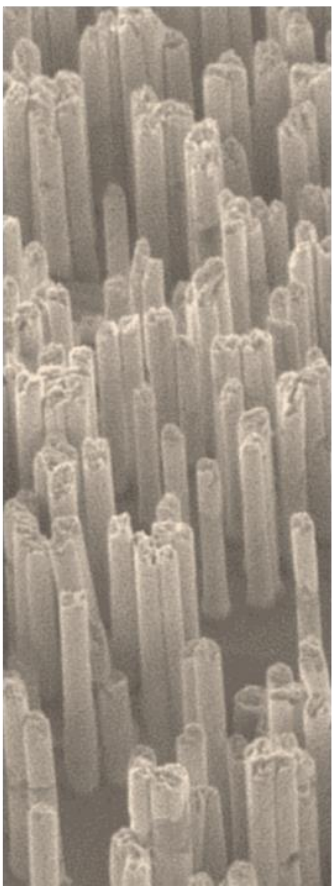

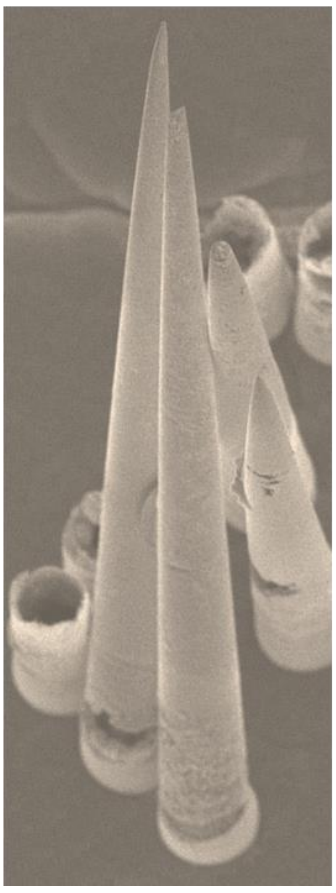

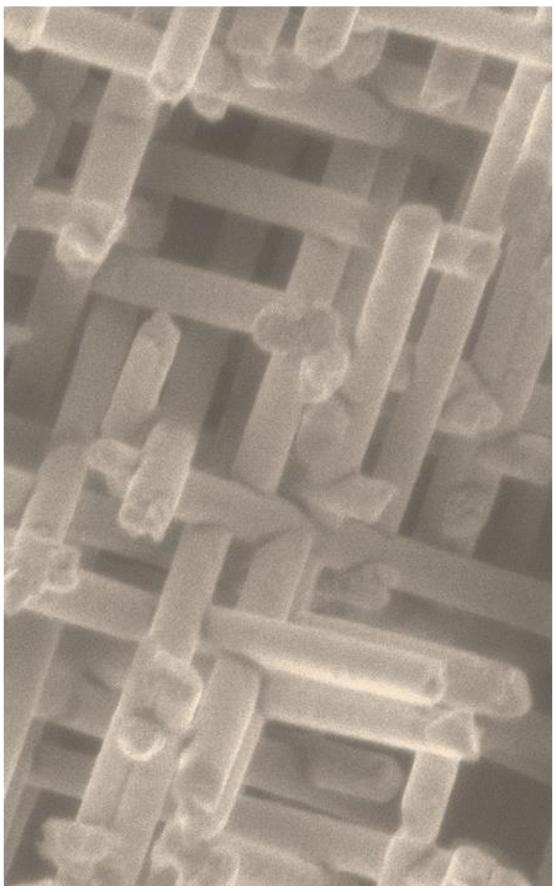

Template-assisted growth and characterization of ZnO-based nanowire arrays and 3D networks

Application of nanowire networks for photoelectrochemical water splitting

Liana Movsesyan

2016

Template-assisted growth and characterization of ZnO-based nanowire arrays and 3D networks: application of nanowire networks for photoelectrochemical water splitting

Template-gestütztes Wachstum und Charakterisierung von ZnO-basierten Nanodrahtarrays und 3D Netzwerken – Anwendung der Nanodrahtnetzwerke für die photoelektrochemische Wasserspaltung

Genehmigte Dissertation von M.Sc. Liana Movsesyan aus Jerewan (Armenien)

1. Gutachten: Prof. Dr. Christina Trautmann

2. Gutachten: Prof. Dr. Wolfram Jaegermann

Tag der Einreichung: 19. Juli 2016

Tag der Prüfung: 06. Oktober 2016

Darmstadt – D17

Bitte zitieren Sie dieses Dokument als:
URN: urn:nbn:de:tuda-tuprints-54424
URL: http://tuprints.ulb.tu-darmstadt.de/5442/4

Dieses Dokument wird bereitgestellt von tuprints,
E-Publishing-Service der TU Darmstadt
http://tuprints.ulb.tu-darmstadt.de
tuprints@ulb.tu-darmstadt.de

Die Veröffentlichung steht unter folgender Creative Commons Lizenz:
Namensnennung – Keine kommerzielle Nutzung – Keine Bearbeitung 4.0 International
https://creativecommons.org/licenses/by-nc-nd/4.0

Erklärung zur Dissertation

Hiermit versichere ich, Liana Movsesyan, die vorliegende Dissertation ohne Hilfe Dritter und nur mit den angegebenen Quellen und Hilfsmitteln angefertigt zu haben. Alle Stellen, die aus den Quellen entnommen wurden, sind als solche kenntlich gemacht. Diese Arbeit hat in dieser oder ähnlicher Form noch keiner Prüfungsbehörde vorgelegen.

Datum: 19.07.2016 Unterschrift:

I herewith formally declare that I have written the submitted thesis independently. I did not use any outside support except for the quoted literature and other sources mentioned in the paper. I clearly marked and separately listed all of the literature and all of the other sources which I employed when producing this academic work, either literally or in content. This thesis has not been handed in or published before in the same or similar form.
In the submitted thesis the written copies and the electronic version are identical in content.

Date: 19.07.2016 Signature:

The work presented in this thesis has been conducted at the Materials Research group of the GSI Helmholtz Center for Heavy Ion Research and was sponsored by the scholarship program from Beilstein Institute for the Advancement of Chemical Sciences (Frankfurt), DFG GRK 1583 and DFG SPP 1613 projects

ñWe are visitors here for one hundred years at the very most. During that period we must try to do something good, something useful with our lives. If you contribute to other people's happiness, you will find the true me

Dalai Lama XIV

Table of Contents

Abstract

In recent years, research on the fabrication of semiconductor nanowires attracted increasing interest in various fields of research. Especially, the successful synthesis of ZnO micro- and nanoscale structures has paved the way to numerous applications for devices including nanogenerators, sensors, solar and fuel cells.

This work focuses on the synthesis of ZnO nanowire arrays and nanowire networks by means of electrochemical deposition in etched ion-track membranes. Three different geometries of nanowire-based structures are discussed: arrays of vertically aligned (1) cylindrical ZnO nanowires and (2) ZnO nanocones as well as (3) mechanically stable three-dimensional (3D) ZnO and ZnO/TiO_2 nanowire networks.

To establish a reproducible growth process of ZnO in track-etched membranes, the electrodeposition parameters of vertically aligned cylindrical ZnO nanowires are adjusted by independently varying the applied potential during the electrodeposition, the pore diameter of the membranes, and the concentration of the electrolyte ($Zn(NO_3)_2 \cdot 6H_2O$). The influence of these parameters on the morphological and crystallographic properties of the nanowires is analysed by means of high resolution scanning electron microscopy (HRSEM) and X-ray diffraction (XRD). ZnO nanocone arrays with µm-size bases and nm-size tips are fabricated applying two growth approaches: base-to-tip and tip-to-base. The arrays are analysed by SEM in terms of mechanical stability.

An important part of this thesis is the design and synthesis of 3D ZnO nanowire networks. The number density and diameter of the nanowires in the network are optimized in order to obtain mechanically stable 3D building blocks exhibiting a high surface area. The crystallographic properties are studied by XRD, high resolution transmission electron microscopy (HRTEM), selected area electron diffraction (SAED) and high-angle annular dark-field (HAADF) imaging. Knowledge drawn from these investigations is crucial for the implementation of these 3D nanoarchitectures into devices, including photodiodes and electrodes.

Furthermore, the durability of ZnO-based nanowire networks in aqueous environment under applied potential and illumination is tested. In particular, they are employed as photoanode model systems for photoelectrochemical water splitting. The measurements are performed on pure ZnO and core/shell ZnO/TiO_2 nanowire networks and compared to those of their film counterparts. The role of the TiO_2 layer as a protection layer against photo(electro)chemical corrosion of ZnO as well as the efficient charge separation and transport from nanowires to the electrolyte is highlighted.

By using X-ray photoelectron spectroscopy (XPS) the contamination and chemical composition on the surface of the networks are quantified before and after photoelectrochemical measurements. Additionally, the Schottky barrier height formed at the

ZnO-Au and TiO_2-Au contacts are theoretically determined from the values of the work function and the valence band position.

The work presented in this thesis shows how the outstanding flexibility of the ion-track technology combined with electrochemical deposition leads to new options for fabrication of complex ZnO-based nanowire structures. The possibility to tune the length, diameter and orientation allows the production of free-standing, high aspect ratio structures which are promising for a wide range of applications, including energy conversion and storage.

Zusammenfassung

In den letzten Jahren hat die Herstellung von Halbleiter-Nanodrähten zunehmendes Interesse in verschiedenen Forschungsgebieten geweckt. Insbesondere eröffnet die erfolgreiche Synthese von ZnO Mikro- und Nanostrukturen eine Vielzahl von Anwendungen, wie z.B. Nanogeneratoren, Sensoren, Solar- und Brennstoffzellen.

Die vorliegende Arbeit konzentriert sich auf die Synthese von ZnO Nanodrahtarrays und Nanodrahtnetzwerken mittels elektrochemischer Abscheidung in geätzten Ionenspurmembranen. Drei verschiedene Geometrien von Nanodraht-basierten Strukturen wurden abgeschieden und analysiert: vertikal ausgerichtete Arrays von (1) zylindrischen und (2) konischen ZnO Nanodrähten sowie (3) mechanisch stabile dreidimensionale (3D) ZnO und ZnO/TiO_2 Nanodrahtnetzwerke.

Um einen reproduzierbaren Wachstumsprozess von ZnO in Ionenspurmembranen zu erzielen, wurden die Abscheideparameter für vertikal ausgerichtete zylindrische ZnO Nanodrähte sowie die angelegte Spannung, der Durchmesser der Poren in den Membranen, und die Konzentration des Elektrolyten ($Zn(NO_3)_2 \cdot 6H_2O$) unabhängig voneinander variiert. Der Einfluss dieser Parameter auf die morphologischen und kristallographischen Eigenschaften der Nanodrähte wurde mittels hochauflösender Rasterelektronenmikroskopie (HRSEM) und Röntgenbeugung (XRD) analysiert. Konische ZnO Nanodrahtarrays mit µm breiten Basen und nm großen Spitzen wurden mit zwei verschiedenen Wachstumsmethoden hergestellt: von der Basis zur Spitze und umgekehrt von der Spitze zur Basis. Mit Hilfe von Rasterelektronenmikroskopie wurde sichtlich ihrer mechanischen Stabilität untersucht.

Ein wichtiger Teil dieser Arbeit ist die Entwicklung und Synthese von 3D ZnO Nanodrahtnetzwerken. Die Anzahl und der Durchmesser dieser Nanodrähte wurden optimiert, um mechanisch stabile 3D Strukturen mit hoher Oberfläche zu erhalten. Die Kristallstruktur wurde mittels XRD, hochauflösender Transmissionselektronenmikroskopie (HRTEM), Feinbereichsbeugung (SAED) und Ringdunkelfeldabbildung (HAADF) untersucht. Die hierdurch erhaltenen Erkenntnisse sind wichtig für die Implementierung dieser 3D Nanoarchitekturen in komplexere Bauteile wie z.B. Photodioden- und -elektroden.

Die Lebensdauer von ZnO-basierten Nanodrahtnetzwerken in wässriger Umgebung wurde bei angelegter Spannung und unter künstlichem Sonnenlicht (Simulator, AM 1.5) getestet. Die Netzwerke dienten als Modellsystem für Photoanoden zur photoelektrochemischen Wasserspaltung. Die Messungen wurden für reine ZnO und Core/Shell ZnO/TiO_2 Nanodrahtnetzwerke durchgeführt und mit den entsprechenden Filmen verglichen. Die Rolle der TiO_2 Schicht als Schutzschicht gegen photo(elektro)chemische Korrosion von ZnO sowie für eine effiziente Ladungstrennung und -transport aus den Nanodrähten zum Elektrolyten wird erörtert.

Mittels Röntgenphotoelektronenspektroskopie (XPS) wird die Kontaminationen und die chemische Zusammensetzung der Oberfläche der Nanodrahtnetzwerke vor und nach photoelektrochemischen Messungen quantifiziert. Zusätzlich werden die Höhen der Schottkybarriere an den ZnO-Au und TiO_2-Au Kontakten aus den Werten der Austrittsarbeit und Valenzbandposition theoretisch bestimmt.

Die durchgeführten Arbeiten zeigen, wie die große Flexibilität der Ionenspurtechnologie in Verbindung mit elektrochemischer Abscheidung zu neuen Verfahren zur Herstellung komplexer ZnO-basierter Nanodrahtsysteme führen kann. Die Möglichkeit die Länge, den Durchmesser und die Orientierung dieser Nanodrähte frei wählen zu können, erlaubt die Herstellung freistehender Strukturen mit hohem Aspektverhältnis, die für ein breites Spektrum von Anwendungen, wie z.B. für Energieumwandlung und -speicherung, geeignet sind.

Introduction

Nanoscale engineering is one of the most prominent and actual research topics nowadays. The demand for more advanced and next-generation devices leads to extensive research effort in nanoscale technology. For miniaturization and increasing of the device efficiency, one-dimensional nanowires are of great interest. In particular, nanowires are excellent model systems for the investigation of size and geometry effects on physical characteristics such as optical,[1–6] electrical,[7–10] magnetic,[11–14] electronic,[15–17] and thermal[18–20] properties. In addition, the integration of nanowires into micro- and macro-devices requires the development of strategies to assemble them into three-dimensional (3D) building blocks with enhanced mechanical stability, flexibility and high surface area.

ZnO micro- and nanoscale structures have attracted tremendous interest for numerous applications. Studies on ZnO nanostructures are motivated by the technologically relevant properties of ZnO including transparency, piezoelectricity, natural n-type conductivity, high thermal stability, high electron mobility (>1000 $cm^2/(V \cdot s)$), a wide and direct band gap of 3.3–3.6 eV, as well as a large exciton binding energy of 60 meV.[21,22] Additional advantages of ZnO include its non-toxicity as bulk material, low cost, and the wide availability on the earth. These properties make ZnO nanowires promising for the integration in a wide range of devices including transistors,[23] sensors,[24,25] nanogenerators, piezoelectric devices,[26] solar cells,[23,27,28] and photoelectrodes for water splitting when protected and/or integrated in tandem cells.[29,30] The application of ZnO in photodetectors, light-emitting diodes, and laser diodes that operate in the blue and ultraviolet region of the light spectrum are also being studied.[31–33] ZnO nanowires embedded in membranes may for example serve as X-ray detectors.[34]

ZnO nanostructures are fabricated by top-down methods including electron beam and optical lithography,[35,36] as well as by bottom-up methods such as sol–gel synthesis,[37] metal organic chemical vapor deposition,[38] and electrodeposition from a seed layer.[39] However, a large scale production of ZnO wires with these techniques is limited by several factors, including time and cost efficiency or control and tuning of nanowire size and geometry. Template-assisted electrodeposition combines both approaches, top-down and bottom-up, and enables the synthesis of nanowires with simultaneous and precise control over length, diameter, and composition.[40–43] The template method has demonstrated to be very suitable for the fabrication of metal and semimetal nanostructures with tuned size and crystallinity. By adjusting the growth parameters, Tornimil-Molares *et al.* showed that it is possible to grow both single and polycrystalline Cu nanowires inside polycarbonate etched ion-track membranes.[44] Pan *et al.* reported the synthesis of single crystalline Ni and Co nanowires in anodic aluminum oxide (AAO) templates.[45] However, reports on the electrodeposition of semiconductor nanowires in polymer templates are rather limited, in particular for ZnO. Zhu *et al.* reported the electrodeposition of ZnO nanowires in polymer membranes with large pores of few hundred nm diameter using a $Zn(NO_3)_2$-based electrolyte.[46] Lincot *et al.* studied

the electrochemical growth of ZnO nanowires from $Zn(ClO_4)_2$ electrolyte in AAO templates and compared the results to the growth of pure Zn nanowires.[47] The influence of the applied potential during pulsed electrodeposition on the morphology and crystallographic properties of ZnO films was studied by Manzano *et al.*[48] However, the influence of the potentiostatic deposition conditions on the structure and morphology of ZnO nanowires with various diameters, as reported in this thesis, has not been discussed before. This study is important in order to understand relevant properties such as electrical resistivity, charge carrier generation and transport, and photoluminescence of the wires, which play an important role in the efficiency of ZnO nanowire-based devices.

To date, the synthesis of nanowire and nanorod-based 3D architectures continues being a challenge. The synthesis of tungsten oxide nanowire networks using a thermal evaporation approach was reported by Zhou *et al.*[49] and Ponzoni *et al.*[50] The growth of nanowires along six crystallographically equivalent directions resulted in the intersection of rectangular nanowires and the formation of a network with a junction angle of nearly 90°. These structures showed good crystallinity, however the width of the wires was not controlled, ranging from several tens of nm to 200 nm. Moreover, the size of networks as a continuous system is only 1-10 µm. Wang *et al.* reported the synthesis of ZnO interconnected networks by a high temperature solid-vapor deposition process.[51] The network consisted of nanorods and nanowires with diameters of ~200 nm. These mesh-like structures have a uniform height of 15-20 µm, however they exhibit an inhomogeneous distribution over the substrate. The main drawbacks of this technique are the limited and non-controlled interconnectivity between adjacent nanowires, the large diameter distribution, and the limited height up to 30 µm. Moreover, only a few compounds are endowed with an ability to self-organize in 3D building blocks.

These limitations and challenges can be circumvented by using template-based growth with pre-designed templates, including mesoporous silica, anodic alumina and track-etched polymer membranes. Lu *et al.* performed electrodeposition of different metal and semiconductor networks in 3D mesoporous silica templates.[52] The diameters of the network ligaments ranged from 2 to 20 nm. However, with this technique it is challenging to obtain large scale networks with well-controlled porosity and height thicker than several microns. A successful fabrication of ordered 3D interconnected nanoarchitectures in anodic porous alumina was achieved by Martin *et al.*[53] These templates are prepared by a two-step anodization process and consist of well-defined nanotubular network in the sub-100 nm range. Although the position and amount of junctions can be precisely adjusted by the anodization parameters, the angle between the pores at the junctions is fixed to 90°, and no optimization for this parameter has been reported yet. Additionally, a pore-widening is observed in these networks, which still needs to undergo optimization in order to obtain networks with monodisperse pore diameters.

Among the template-based techniques for fabrication of hierarchal structures, ion-track technology is very attractive because it allows for easy tuning the height (up to 100 µm) and area (up to ~20 cm^2 large) of the network, the diameter (20 to few hundreds of nm), number density (up to 10^{10} cm^{-2}) and interconnectivity of the pores in the template as well as the angle between interconnected pores. 3D structured templates based on irradiation performed at the GSI Helmholtz Center for Heavy Ion Research have been successfully used for electrochemical deposition of Pt,[54] ZnO,[55] and Sb[56] nanowire networks, electroless plating of Au, Ni, Cu, Pt and Ag[57] and atomic layer deposition of Al_2O_3, SiO_2 and TiO_2[58] nanotube networks as well as Pt, Cu and Ag superstructures consisting of interconnected nano- and microscale pores.[59] The compact design, mechanical stability and high surface area of nanowire-based 3D hierarchical systems can be advantageous for example to facilitate efficient light absorption and charge carrier transport in photoelectrodes[30,60–63] and optical elements,[64,65] to enhance the performance of gas sensors,[50,66] batteries[67,68] and supercapacitors[69] or to achieve high electric field confinement and enhancement in 3D plasmonic hollow nanocavities,[70] as well as for computer and chip technologies.[71]

This thesis focuses on the synthesis and characterization of ZnO nanowire-based structures applying ion-track technology in combination with electrochemical deposition. The overall goal of this work has been to optimize ion irradiation, etching and electrodeposition parameters to achieve a reproducible and controlled growth of ZnO nanostructures. Detailed analysis of the shape, size, morphology and crystallinity of the wires is of prime importance for applications.

Three different geometries are studied, namely arrays of vertically aligned cylindrical nanowires and nanocones as well as nanowire networks. It is shown that applying a low concentration of the electrolyte leads to the growth of nanowires with a smooth surface. By varying the applied potential of the electrodeposition, the texture of ZnO wires can be changed. Also, the nanopore diameter is found to be a tool to vary the preferred orientation of the wires. The mechanical stability of cylindrical nanowire arrays after dissolution of the polymer is studied by altering the aspect ratio (length to diameter ratio) of the wires. Membranes with conical pores are employed as template for the electrodeposition of conical ZnO wires. Two growth approaches are discussed, base-to-tip and tip-to-base. In both cases, the arrays are polycrystalline, but the morphology changes significantly depending on the growth direction.

ZnO nanowire networks with different nanowire diameters and number densities are synthesised, and these parameters are optimized to obtain reproducible, free-standing and stable structures. The growth homogeneity of these networks is improved by adding one more irradiation step to the standard network irradiation process and applying a mask with pre-defined areas. Additionally, photoelectrochemical performance of pure ZnO and core/shell ZnO/TiO_2 nanowire networks is tested and compared to their film counterparts, resulting in higher photocurrents for the network structures. The surface imaging before and after

photoelectrochemical measurements shows that the TiO_2 layer protects the ZnO network from corrosion and morphological changes.

The thesis is composed of six chapters. Chapter 1 describes the theoretical background and working principle of the techniques used for this thesis as well as the characteristic parameters of ZnO relevant for the explanation of the results. Chapter 2 introduces the methods of characterization and the measurement tools. Chapter 3 depicts the preparation processes of membranes with vertically aligned cylindrical and conical channels as well as networks of interconnected nanochannels. The main results of the synthesis, growth optimization and characterization of ZnO cylindrical and conical wire arrays as well as nanowire networks are presented in Chapter 4. The characterization of crystallinity and composition of pure ZnO and ALD-coated ZnO/TiO_2 core/shell nanowires and networks is presented in Chapter 5. Lastly, Chapter 6 sheds light on the photoelectrochemical measurements performed with bare ZnO and core/shell ZnO/TiO_2 nanowire networks in order to test their reliability and stability for future applications. The morphology and composition of their surface before and after the measurements is discussed.

1. Theoretical background

This chapter introduces the concepts of the ion track technology and electrochemical deposition in polymeric membranes. The main properties of ZnO, relevant for this thesis, are elucidated. The working principle of photoelectrochemical water splitting and metal semiconductor contacts are described.

1. Theoretical background

1.1. Ion-track technology

When passing through matter, heavy ions dissipate their energy mainly because of elastic and inelastic coulomb interactions with the atoms of the material. If the ion velocity is below 0.01 MeV per nucleon (MeV/u), elastic collisions (nuclear energy loss) dominate whereas at higher ion velocities the interaction is influenced by inelastic collisions that lead to ionization and electronic excitation processes (electronic energy loss). For the fabrication of ion-track membranes swift heavy ions of several MeV/u were used. Thus the energy loss per unit path length (dE/dx) is based on electronic stopping. The energy loss is related to the charge of the ion projectile and is described by the Bethe-Bloch formula:[72]

$$-\frac{dE}{dx} = \frac{4\pi z_{eff}^2 e^4 n_e}{m_e v^2} \left[\ln\left(\frac{2m_e v^2}{I(1-\beta^2)}\right) - \beta^2 \right] \cdot F_1 \cdot F_2 \qquad (1)$$

where m_e is the mass of the electron, v is the velocity of the ion, $\beta = v/c$ (c is the speed of light), z_{eff} is the charge state of the ion, n_e is the number density of the electrons in the material, z_t is the atomic number of the target material, and I is the mean ionization potential of atoms in the target medium, through which the particle is passing, and F_1 and F_2 are correction factors, which take relativistic effects into account. The main conclusions arising from the Bethe-Bloch formula are the following: the energy loss (also called stopping power) depends on the charge of the ion, the electron density in the material, and it is a function of the ion velocity, $v = f(E_{kin}, m_{ion})$. In the case where stopping of the ions in the material is mainly derived from inelastic collisions, nuclear stopping is often ignored. The energy loss of Bi ions in polycarbonate as a function of the ion energy per nucleon calculated by means of the SRIM-2003 code (Stopping and Range of Ions in Matter) is shown in Figure 1a in a double logarithmic scale. The dashed green and red curves correspond to the electronic and nuclear energy losses, respectively, and the solid blue curve represents the total energy loss.

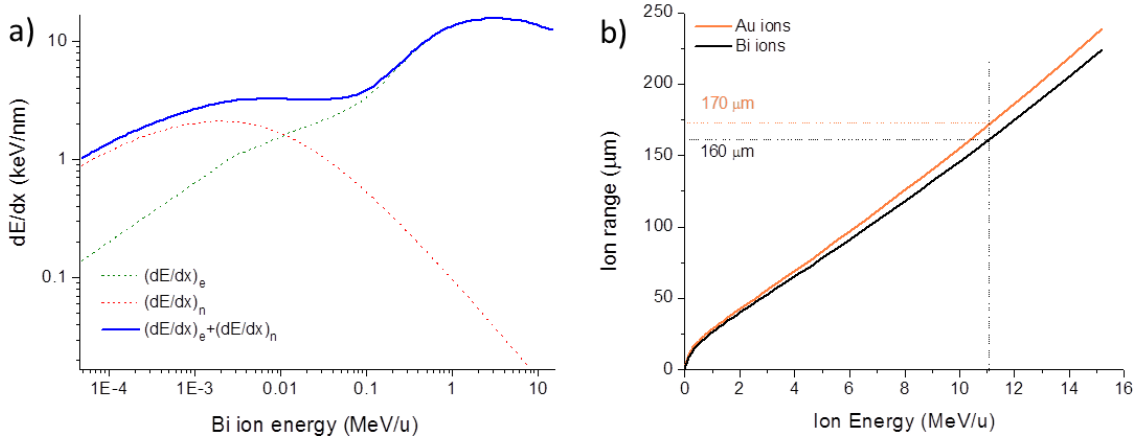

Figure 1: a) Energy loss of Bi ions and b) range of Au (orange) and Bi (black) ions in polycarbonate as a function of the specific ion energy according to the SRIM-2003 code simulation.

The complete penetration depth (R_p) of the ion with initial energy E_0 can be determined from the following expression[73]

$$R_p \approx \frac{0.9}{\left(\frac{dE}{dx}\right)_{e,0}} \cdot \frac{E_0}{1 + \frac{\left(\frac{dE}{dx}\right)_{e,0}}{\left(\frac{dE}{dx}\right)_{n,0}} \cdot \frac{M_2}{M_1}} \quad \text{with} \quad \left(\frac{dE}{dx}\right)_{e,0} = k \cdot E_0 \tag{2}$$

where $(dE/dx)_e$ and $(dE/dx)_n$ are the electronic and nuclear energy losses per unit path length, respectively. The range of Au and Bi ions (which were used in this work) in polycarbonate foils calculated using the SRIM-2003 code is presented in Figure 1. The dashed lines correspond to the values of penetration range and energy of Bi (black) and Au (orange) ions, being 160 and 170 µm for Bi and Au ions with an energy of 11.1 MeV/u, respectively. Considering the penetration range of the ion, polymer foils which have thicknesses of few tens µm can be assembled in stacks so that several foils are irradiated in one step.

Depending on the ion energy and the charge state, the ion energy loss produces structural defects and compositional variations in the polymer. The radiation damage formed along the trajectory of each incident ion is called latent track. Tracks have commonly a cylindrical geometry and a diameter between 5 and 10 nm depending on ion energy loss and target material. In polymers, the energy loss of heavy ions leads to breakage of the chemical bonds, amorphization and outgassing of small volatile fragments.[74,75]

Schematic representation of the irradiation process is shown in Figure 2. The swift heavy ions used for irradiation at the UNILAC provide highly aligned parallel tracks. The beam incidence can be varied from normal to the sample surface down to grazing angles. In contrast to commercial ion-track membranes, those fabricated at the GSI are characterized by a very small angular spread

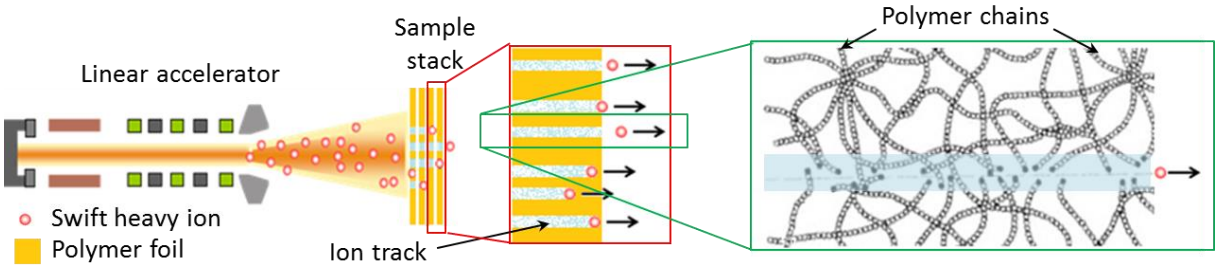

Figure 2: Schematic representation of the linear accelerator (UNILAC) at the GSI and the irradiation process of a stack of polymer foils under normal incidence. The zoomed-in images show schematically a single track consisting of broken bonds of polymer chains (adapted from[43,72]).

By means of chemical etching, the irradiated foils are converted to porous membranes by selectively removing the damaged material and thereby converting each ion track into an individual open pore. Since each ion creates one track, the number of the pores in the membrane is equal to the ion fluence (number of ions per cm^2). The size and homogeneity of the etched pores depend on the properties of the target material (e.g. density, composition, crystallinity), the energy loss of the ions, the etching time and etching solution. In addition, to

obtain pores with uniform diameter and well defined shape, the etching rate along the damaged ion track (v_t) should be much higher than the isotropic etching rate of the non-damaged bulk material (v_b). The v_t/v_b ratio will determine the opening angle of the pore.[76,77,78] If $v_t >> v_b$, the resulting pores have a cylindrical shape, whereas conical pores are achieved in the case of a smaller etching rate ratio. The fabrication process of membranes with parallel cylindrical and conical pores as well as with interconnected nanopore networks are described in detail in Chapter 3. It is important to mention that, prior to etching, both sides of all irradiated polymer foils used for experiments in this thesis were exposed to UV light in air. It is known, that UV irradiation modifies the chain compounds inside the track without significant effects on the virgin PC thus improving the diffusion of the etching solution along the track. Besides, it triggers creation of new chain ends and acidic compounds which are highly sensitive to etchant. As a result, UV treatment affects the etching rate and improves its selectivity and the monodispersity of the nanopores.[79,80,81]

1.2. Electrodeposition

The template method, and in particular electrodeposition in etched ion-track membranes, combines both top-down and bottom-up approaches and has demonstrated to be a very appropriate technique for the growth of nanostructures with small size and high surface-to-volume ratio.[20,22] It enables the synthesis of nanowires and nanotubes with simultaneous and excellent control over length and diameter. The template method has demonstrated to be very suitable for the fabrication of metal and semimetal nanostructures with tuned size, composition, and crystallinity.[21,23] Besides continuous single component wires, also segmented as well as multicomponent[23,82] and alloy[83,84] structures can be fabricated.

Electrodeposition of micro- and nanowires is carried out using electrochemical cells consisting of two or three electrodes which are connected to a potentiostat for controlling and measuring the current and potential. The setup can be operated either in potentiostatic (constant applied potential) or galvanostatic (constant applied current) mode, as well as in pulsed electrodeposition conditions (pulsed applied potential). In this work, potentiostatic growth in a three-electrode configuration is applied. This method allows for a precise control of the composition of the deposit not only for one but also for multicomponent materials with a chosen stoichiometry.[84]

The thermodynamic potential needed for the electrochemical reactions is determined by the Nernst equation, which describes the redox potential E_{redox} of a redox couple by the following equation:[85]

$$E_{redox} = E^0 + \frac{RT}{zF} \ln \frac{a_{ox}}{a_{red}} \qquad (3)$$

where E^0 is the standard electrode potential of the redox couple with respect to the normal hydrogen electrode (NHE), and a_{ox} and a_{red} are the activities of the oxidized and reduced

species, respectively. *R* is the gas constant (8.3145 J/mol·K), *T* is the temperature, *z* is the number of electrons involved in the reaction, and *F* is the Faraday constant (96485 C/mol). Thermodynamically, when the potential applied to the working electrode is more negative than $E^0_{M^{z+}/M}$ (in case of reduction), electrodeposition takes place and the ions in the electrolyte are reduced and may form a solid material on the working electrode.

In the simplest case of metals, electrodeposition is a process of reducing metal ions from an aqueous solution upon application of a potential. When the current flows from the counter electrode to the working electrode, the metal ions (M^{z+}) in the electrolyte that travel to the working electrode are reduced on the metallic substrate by capturing electrons. The corresponding reaction that takes place is as follows:[85]

$$M^{z+} + ze^- \rightarrow M \quad (4)$$

The schematic of the electrochemical cell with the three electrode (working, counter and reference electrodes) connected to the potentiostat is shown in Figure 3. The membrane with sputtered and electrodeposited metallic layers on one side always acted as a working electrode, which was in contact with the copper ring of the cell. As counter electrode a platinum wire and as reference electrode a Ag/AgCl (sat. KCl) were used. In this setup, the potential is applied to the working electrode with respect to the reference electrode. The fixed potential of the Ag/AgCl reference electrode (0.197 V vs. the standard hydrogen electrode at 25 °C)[86] allows reproducibility for all experiments.

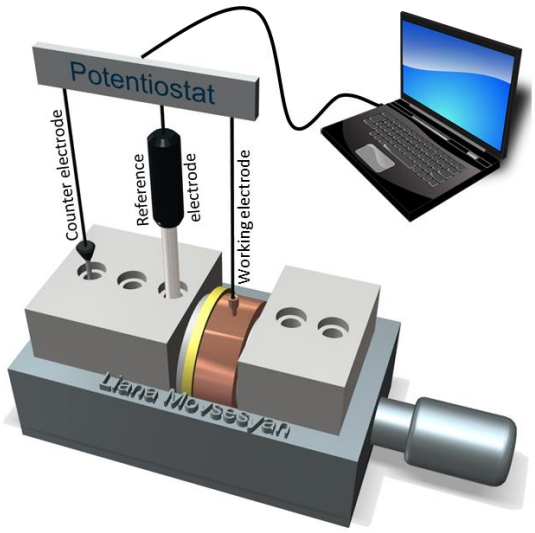

Figure 3: Schematic of electrochemical cell for nanowire growth by using three electrodes (working, counter, and reference) connected to a potentiostat, which is controlled via computer. The metallic layer sputtered and electrodeposited on one side of the membrane served as a working electrode.

The growth process was monitored and controlled by recording chronoamperometric (current vs. time) curves during electrodeposition, which enabled us to monitor the different growth steps during the synthesis process (Figure 4).

The charge and mass transfer of the deposit material are quantified with Faraday's law, which states that the mass (m) of the deposited material is directly proportional to the total amount of transferred charge

$$m = \frac{M}{zF} \int_{t_0}^{t_n} I \, dt \qquad (5)$$

where I is the current passing through the circuit during the time period between t_0 and t_n, M and z are the molar mass and valence of the deposited atoms, respectively, and F is Faraday constant. With this formula, the amount of deposited material can be calculated from the I-t curves recorded during electrodeposition process. Figure 4 presents a typical chronoamperometric curve for electrodeposition of ZnO in the cylindrical channels of a polycarbonate membrane with an average pore diameter of 250 nm and density of 10^9 pores/cm^2.

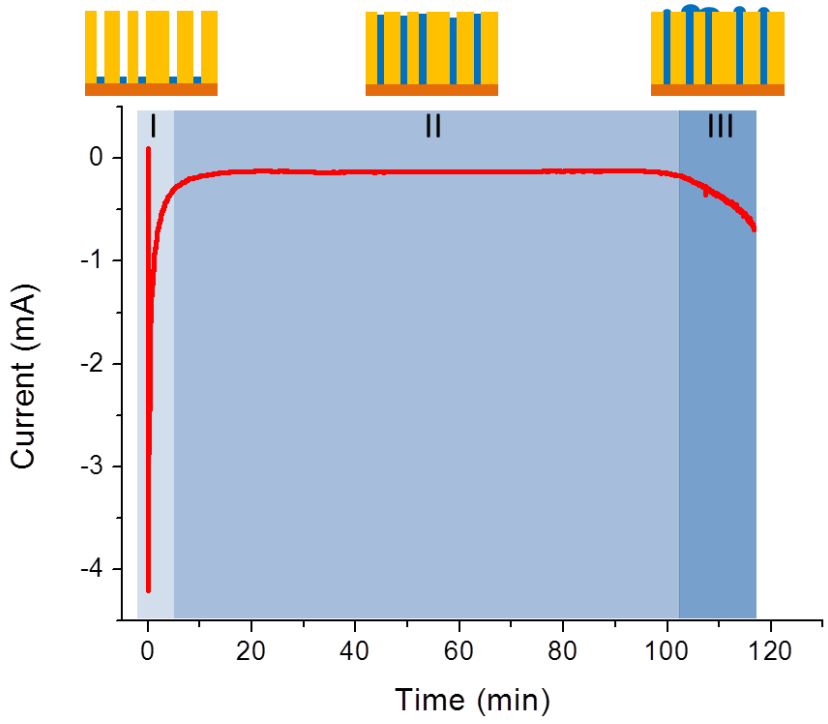

Figure 4: Representative chronoamperometric curve recorded during electrodeposition of ZnO nanowires, showing the dependence of the deposition current with respect to the time, and schematics of three regimes for nanowire growth.

At the beginning of the deposition process (region I), the current rapidly increases (in absolute value) and then decreases during the following few minutes. This effect is attributed to the charging of the double layer (Helmholtz plane) and formation of the diffusion layer, as well as to nucleation processes. As the growth of nanowires inside the membrane pores continues (region II), the current remains almost constant. Finally, when the pores are completely filled, so called caps start to grow on top of the wires, expanding on the surface of the membrane. Caps growth is indicated by an increase in current due to the increased effective area where the

growth takes place (region III).[87] By following this current behavior during nanowire growth, the deposition can be stopped at a defined time period, e.g. to obtain nanowires with the desired length.

In the case of multicomponent materials, such as metal oxides, growth takes place in more than one step depending on the electrolyte composition and pH. For the synthesis of metal oxides, electrodeposition from nitrate based solutions is one of the most common techniques. The driving force in this process is the nitrate reduction which leads to a local pH increase in the electrolyte due to formation of OH^- ions. In this work, an aqueous electrolyte of zinc nitrate hexahydrate ($Zn(NO_3)_2 \cdot 6H_2O$) was used for the growth of ZnO nanowires, which takes place in several steps. First, upon application of the potential, hydroxyl ions (OH^-) are formed at the cathode/electrolyte interface according to reaction 6. In the presence of Zn^{2+} ions in the solution hydroxylation reaction takes place forming $Zn(OH)_2$ (reaction 7). If the electrolyte is heated at elevated temperature, $Zn(OH)_2$ is dehydrated thus resulting in the formation of fully crystalline ZnO according to reaction 8. As mentioned before, the local pH in the bath close to the electrode as well as in the pores is increasing because of the formation of OH^- ions, leading to the preferential growth of ZnO inside the pores of the membrane. Depending on the ratio of the produced OH^- and Zn^{2+} ions and the supersaturation in the bath, the crystal growth will behave differently leading to different crystal orientations. Therefore, the crystallinity depends on the concentration of OH^- ions.[39,55,88]

$$NO_3^- + H_2O + 2e^- \rightarrow NO_2^- + 2OH^- \quad (6)$$

$$Zn^{2+} + 2OH^- \rightarrow Zn(OH)_2, \quad (7)$$

$$Zn(OH)_2 \xrightarrow{\Delta} ZnO + H_2O \quad (8)$$

Previous studies reported the electrodeposition of ZnO nanostructures from $Zn(NO_3)_2 \cdot 6H_2O$ with pH values adjusted between 7 and 11 by adding NaOH to the electrolyte.[89–91] To avoid degradation of the polymer by high pH electrolytes during nanowire growth, an as-prepared electrolyte with pH 5 was used in this work. The growth process took place for parallel arrays and nanowire networks, respectively.

1.3. Structural and physical properties of ZnO

During the past few years, the research activities on zinc oxide (ZnO) have significantly increased. The history of the research on ZnO goes back to 1930s reaching its peaks in the late 1960s due to the availability of single crystalline bulk ZnO produced by chemical vapor deposition (CVD).[92,93] Although ZnO is the oldest known compound material, still numerous questions about the structural and optical properties of this material. Particularly, nanoscale 1D structures, such as nanowires, nanobelts, nanoflowers, nanoribbons, nanorods, nanowalls, and nanotubes drastically attracted the attention of scientists due to their promising application in technology.[23]

1.3.1. Crystal structure

ZnO can crystallize in three possible polymorphs wurtzite, rocksalt and zinc-blende. Thermodynamically the most stable phase is the wurtzite crystal structure, where each Zn atom is surrounded by a tetrahedron of four oxygen atoms, and vice versa. The wurtzite structure has a hexagonal unit cell with two lattice constants a = 0.3249 nm and c = 0.5204 2 nm at ambient conditions, and belongs to the $P6_3mc$ space group.[94] The structure consists of interpenetrating hexagonal close-packed (hcp) bi-layers of zinc and oxygen displaced with respect to each other along the c-axis.[94] The schematic representation of the ZnO wurtzite lattice with the primitive cell is shown in Figure 5a. The crystallographic orientations of the a- and m-planes are highlighted in Figure 5b. The directions and planes for hexagonal structures are indexed either with three digit Miller indices (hkl) or four digit Bravais-Miller indices (hkil). For ZnO, it is more common to use the four axes a_1, a_2, a_3 and c, and therefore four indices, where h, k and i are related as follows: h+k = -i. This relation allows the transformation of Miller to Bravais-Miller indices, and vice versa. The c-axis is always referred to as the [0001] direction, and the planes perpendicular to this axis are the hexagonal (0001) planes. The latter are the most commonly observed facet and the main polar surface in wurtzite ZnO arising from the strong bond polarity of Zn^{2+} and O^{2-} ions, being either zinc or oxygen terminated. Other planes also often observed in wurtzite ZnO are {$2\bar{1}\bar{1}0$} and {$01\bar{1}0$}, which are non-polar surfaces due to the equal amount of Zn and O.[23,27,94-96]

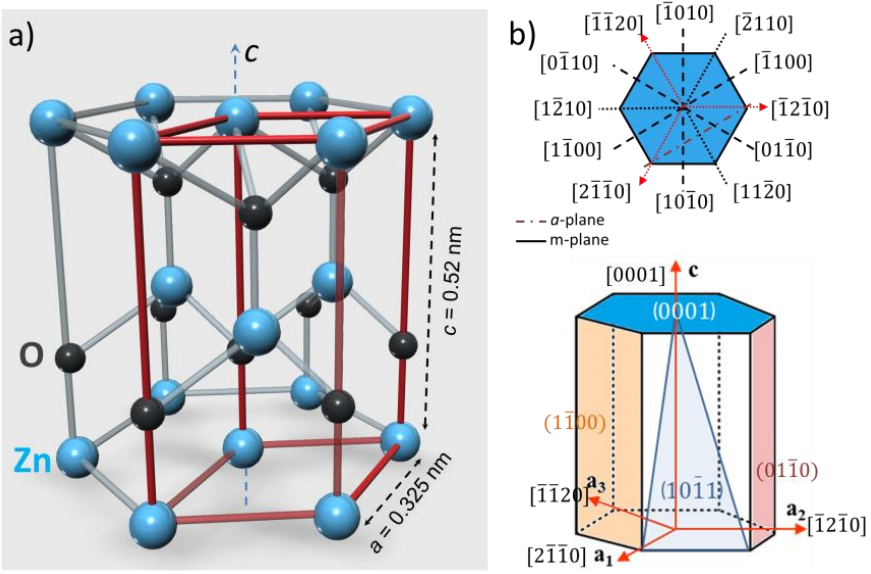

Figure 5: a) Schematic representation of the wurtzite ZnO structure with a primitive cell, b) crystallographic orientations of planes that are commonly present in the wurtzite phase.

1.3.2. Band structure

ZnO is a II-VI semiconductor with a wide band gap (E_g) of 3.37 ± 0.01 eV at room temperature, which is in the near UV-spectral range.[94] The first theoretical and experimental

studies of the electronic band structure of ZnO go back to the late 1960s and 1970s.[85,97,98] Energy bands of hexagonal ZnO as shown in Figure 6.[97] Both the valence band (VB) maximum and the conduction band (CB) minimum are positioned at the same point with k = 0 wave vector, indicating that ZnO has a direct band gap. Several theoretical and experimental works have shown the presence of *d* bands in ZnO at around 6 - 9 eV below the VB, which correspond to Zn *3d* orbitals. Due to the significant overlap of d orbitals, ZnO has broader *d* bands than any other II-VI compound.[97] The states closer to the VB maximum correspond to O *2p* orbitals, whereas the O *2s* bands are situated far below the VB (at ~20 eV). The CB is formed mainly by the empty Zn *4s* levels.[99,100] The bonds in wurtzite ZnO have sp^3 covalent nature.

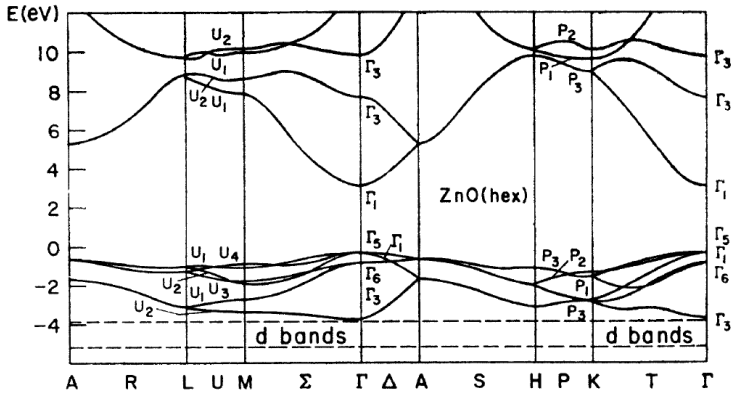

Figure 6: Energy band of hexagonal ZnO according to Rössler (1969)[97]

Among all II-VI compounds, ZnO has the largest excitation binding energy of 60 meV,[21,22] which makes ZnO a very interesting material for photonic devices due to its broad emission band.

1.3.3. Electrical properties

Both theoretical and experimental studies on the electrical properties of ZnO films and nanostructures have been reported since a few decades. Because of the oxygen vacancies in the structure, normally undoped ZnO has intrinsic n-type conductivity. The more oxygen vacancies are present, the higher is the electron density. As compared to other II-VI semiconductors, bulk ZnO has a very high electron mobility (~200 $cm^2V^{-1}s^{-1}$ at 300 K, ~2000 $cm^2V^{-1}s^{-1}$ at 50 K),[101] which is expected to improve the performance of electronic devices based on this material. A higher electron Hall mobility was reported in studies of ZnO/Mg:ZnO heterostructures reaching up to 5500 $cm^2V^{-1}s^{-1}$.[102] For transparent conductive oxide devices, ZnO is often doped with group III metals like Al, Ga, and In, which enhances the n-type conductivity of ZnO.[103–105] For a long time, intensive efforts have been put in research on the synthesis of p-type ZnO, which is one of the main challenges of this material. p-ZnO is mainly obtained by doping with phosphorus[106] or nitrogen.[107,108] Despite the vast number of reports, the fabrication of p-type ZnO is hardly reproducible.

1.4. Photoelectrochemical water splitting

One of the most important but challenging technological issues of the century is the shift from fossil fuels to renewable energy sources, such as hydro and wind power, solar energy, and biofuels. The main problems related to the use of fossil fuels such as coal, natural gas and oil products are the release of CO_2 gas to the atmosphere and the limited and quickly diminishing amount of fossil fuel sources on earth. Renewable energy sources have great potential to substitute fossil fuels and serve as an infinite sustainable energy source providing a clean environment. Large scale research has been performed and is ongoing worldwide in search of environmentally friendly energy sources. In 1883, the first solar cell based on selenium was made by Charles Fritts. However, this solar cell did not have a large scale use because of the sunlight to electricity conversion efficiency being less than one percent. In 1954, the first practical Si-based solar cell was demonstrated in the Bell laboratories by Daryl Chapin, Gerald Pearson and Calvin Fuller with an efficiency of about six percent. This was the highest reported value at that time. The efforts to produce photovoltaic devices with high efficiency still continue at present.

A new approach to obtain a clean, cost efficient and domestically produced energy source was proposed by Akira Fujishima and Kenichi Honda in 1972[109]. They demonstrated the first successful experiment of light-assisted water splitting using an n-type TiO_2 photoanode connected with a platinum black electrode in a photoelectrochemical (PEC) cell for hydrogen production as a renewable energy source. Since then, many efforts have been devoted to this research field. More efficient water splitting systems have been obtained by combining several materials such as a tandem cell, adding co-catalysts, and applying different configurations of PEC cells[110–113]. Albeit increasing the efficiency of both photon-to-current conversion and generation and collection of hydrogen remain challenging, light-driven PEC water splitting for hydrogen production is one of the most promising and dominating fields of research today.

The principle of the PEC cell is based on the physics of semiconductor-light interaction. Important parameters to be considered during the choice of the materials are

- the band gap of the semiconductor has to be small enough to absorb light in a relatively wide range of the solar spectrum,
- the position of the CB minimum and VB maximum with respect to the hydrogen and oxygen redox potentials for efficient hydrogen and oxygen evolution reaction (HER and OER, respectively), i.e. the CB minimum must be higher in energy than the standard redox potential of H^+/H_2 couple, and the VB maximum must be lower than the standard redox potential of the H_2O/O_2 couple,
- the stability against the (photo)electrochemical corrosion in aqueous electrolytes,

- efficient separation and transfer of minority charge carriers from the core of the photoelectrode to the semiconductor/electrolyte interface, and of the majority charge carriers to the counter electrode, with minimum recombination

A vast variety of single-, bi- and multicomponent materials, such as ZnO:Al, ZnO, TiO_2, Cu_2O, Fe_2O_3, WO_3, GaP, GaN, Si, CdS, CdSe, $BiVO_4$, $NaTaO_3$:La and many others, have been studied.[114–118] The standard redox potential of the H_2O/O_2 couple is 1.23 V versus the reversible hydrogen electrode (RHE), which means that the band gap of the photoelectrode material must be larger than this thermodynamic minimum value of potential for splitting the water. The positions of several common semiconductors with respect to the redox potentials for water splitting are shown in Figure 7a.

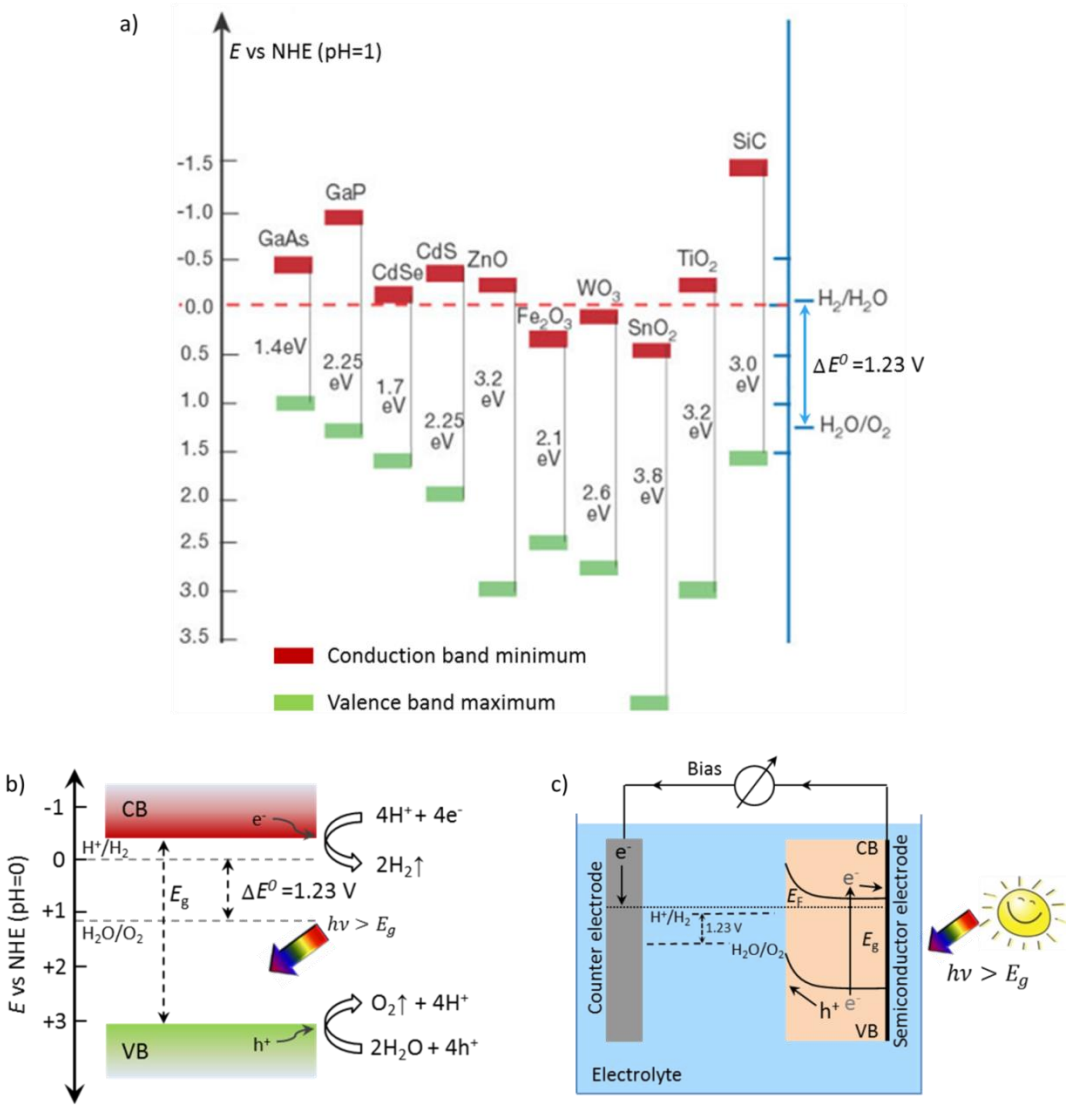

Figure 7: a) Relation between the band position of different semiconductors and redox potent water splitting (adapted from[119] with permission), b) schematic representation of the band structu ZnO under illumination together with the hydrogen and oxygen evolution reactions, c) simplif schematic of a PEC cell with n-type photoanode and metallic counter electrode

The basic principle of the overall water splitting process is schematically shown in Figure 7b. When a semiconductor photoelectrode is illuminated, the absorbed photons with higher energy than the band gap energy excite electrons into the CB thus forming electron-hole pairs, which are separated by the formed electric field in the depletion layer. If the semiconductor is immersed into a water-based electrolyte, the holes from the VB will drive the OER producing oxygen gas, and electrons from the CB will lead to the formation of hydrogen by the HER according to the following reactions:

$$2H_2O + 4h^+ \rightarrow O_2 + 4H^+ \quad (9)$$

$$4H^+ + 4e^- \rightarrow 2H_2 \quad (10)$$

The semiconductor serves as a photoanode in a PEC cell if it has n-type conductivity (electrons are the majority charge carriers) and as a photocathode if the conductivity is p-type (holes are the majority charge carriers). The schematic of a simple PEC cell with an n-type photoanode, like ZnO, is shown in Figure 7c. The cell consists of the semiconductor photoelectrode (working electrode), a metal counter electrode, which is typically Pt, and a reference electrode required to control the potential of the working electrode (not shown in the schematic). If a bias is applied, the photogenerated electrons and holes will separate and migrate through the semiconductor in opposite directions: the holes will travel to the surface of the n-type semiconductor, where the OER will take place at the electrode/electrolyte interface, and electrons will travel through the external circuit to the counter electrode driving the HER.[118] It is common to use a Ag/AgCl reference electrode for measurements, whereas for data analysis and for ease of comparison with other systems reported in literature, the Nernst equation is used to convert the potentials vs. reversible hydrogen electrode (RHE):

$$E_{RHE} = E_{Ag/AgCl} + E^0_{Ag/AgCl} + 0.059 \times pH \quad (11)$$

where E_{RHE} is the converted potential vs. RHE, $E_{Ag/AgCl}$ is the potential applied externally vs. the Ag/AgCl (sat. KCl) reference electrode used, and $E^0_{Ag/AgCl} = 0.197$ V is the standard potential of a Ag/AgCl reference electrode at 25 °C.[86]

To improve the efficiency of PEC cells, the possible recombination of photogenerated charge carriers travelling to the semiconductor surface or counter electrode should be minimized. For this, nanowire-based photoelectrodes are of interest due to their one-dimensional shape and geometrical orientation which promise higher light absorption and more efficient charge carrier separation and transport to the surface of the electrode as compared to bulk materials.[120–122] The reduced nanowire diameter and large surface area of the photoelectrode/electrolyte interface facilitate rapid transport of photogenerated charge carriers to the wire surface and faster redox reactions, respectively. For example, the diffusion length of bulk ZnO at 25 °C is ~440 nm which increases with higher temperatures.[123] If a film photoelectrode is much thicker than the diffusion length of the minority charge carriers, in this case holes (L_p), not all holes (especially the ones generated in deeper layers of the

semiconductor) will reach the film surface (Figure 8a). In contrast to this, due to the more available surface area of nanowires, the holes will have a shorter path length to quickly diffuse to the electrode/electrolyte interface, thereby also opening a highway to reach the substrate and flow to the external circuit (Figure 8b). Hence, charge transport limitations can be circumvented by means of adjustment of nanowire diameter. Moreover, enhanced light absorption is expected for nanowires compared to films due to extensive light scattering[124]. The reflected light from one wire can be absorbed by the neighboring wire, and if the photon energy is larger than the band gap energy of the material, the reflected light can also excite electrons into the CB. For this approach, tilted nanowire geometry might be beneficial. Also, a composite structure with wide and narrow band gap materials is of interest. The photons which are not absorbed by the wide band gap material or those that are reflected at the surface can excite charge carriers in the narrow band gap material. Another important parameter that should be considered during the material choice is the optical absorption length, $1/\alpha$, where α is the absorption coefficient. For more efficient devices, the light penetration depth should be comparable with dimensions of the photoelectrode, e.g. film thickness or nanowire diameter.

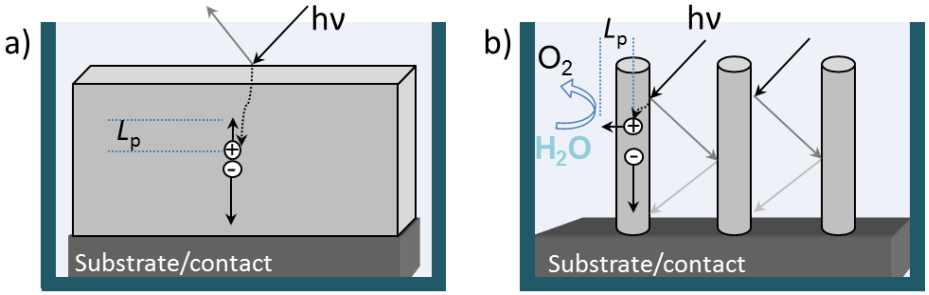

Figure 8: Schematic representation of two photoanodes showing long and short path lengths for photogenerated holes to the electrode surface in a) a film and b) a nanowire array. L_p is the diffusion length to the hole.

One further route to successful transport and collection of photogenerated charge carriers is the use of a photoelectrode with high crystallinity. Electron-hole recombination is less likely to occur in single crystalline structures, whereas the grain boundaries in materials with poor crystallinity are limiting aspects because they serve as traps and recombination centers for electrons and holes[114,124].

Last but not least, the lifetime of the photoelectrodes should be mentioned. Even if the band position of the semiconductor perfectly matches the OER and HER potentials, the photo- and (electro)chemical corrosion should be taken into account, too. This is probably the most severe limitation for the choice of photoactive materials. For most non-oxide materials a decomposition or oxidation of the surface is typical, while for many oxide materials the thermodynamic instability is accompanied with hole oxidization[124]. In particular, ZnO tends to decompose in aqueous solution under illumination following the reaction below[114,125,126]:

ώ è ϋϭ ςΩ^ ο ώ è^ ϭ ρ ς ΰ . ħ (12)

Fortunately, there are several simple oxide semiconductors, such as TiO_2 or SnO_2, which have excellent stability against chemical and photocorrosion in a wide range of pH values of the electrolyte. Coating other photoactive electrodes with these materials can be a solution to extend the lifetime of the device. In this work, ZnO photoanodes were coated with TiO_2 layers of different thicknesses by atomic layer deposition (ALD). The protection role of the TiO_2 layer during PEC measurements is discussed in Chapter 6.

1.5. Metal-semiconductor contact

To describe metal-semiconductor contacts, band diagrams are usually built to visualize the alignment of the bands at the interface of two materials. This section introduces several characteristic parameters for semiconductors used to describe the band diagrams.

A schematic of the band of a metal and an n-type semiconductor (e.g. ZnO, TiO_2) before and after bringing them into contact are shown in Figure 9 (a) and (b), respectively. The band structure of the metal is characterized by its work function W_m. On the diagram, it is the distance between the Fermi level (the highest occupied electron energy level at absolute zero temperature) of the metal and the vacuum level E_{vac}, and represents the amount of the energy that is required to transport an electron from the Fermi level to the vacuum level. The characteristic parameters shown on the diagram for a semiconductor are the following:

- band gap E_g - distance between the minimum of the conduction band (E_c) and the maximum of the valence band (E_v),
- work function W_{sc} - the distance of the Fermi level (E_F) from the vacuum level,
- ionization energy I_{sc} - the distance of the valence band maximum from the vacuum level.

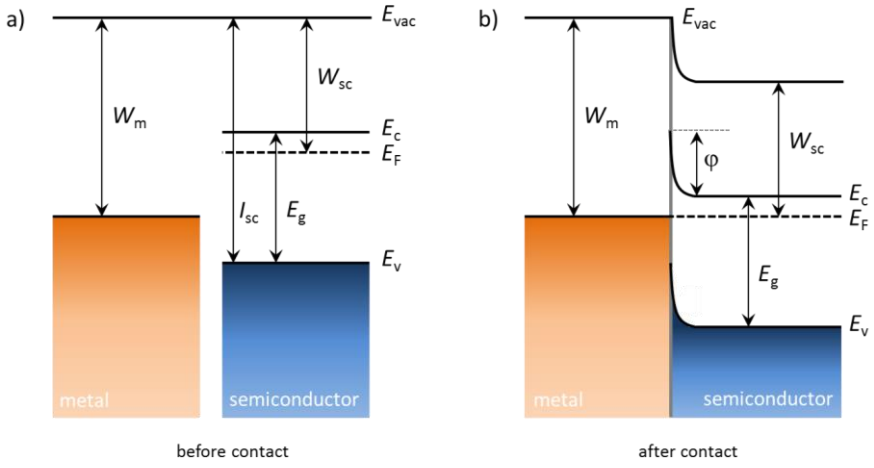

Figure 9: Energy bands for a metal and an n-type semiconductor (a) before and (b) after bringing th into contact. The Fermi level of the metal is lower than that of the semiconductor, i.e. $W_m > W_{sc}$.

Figure 9 shows the case of an n-type semiconductor-metal contact without a bias for which $W_{sc} < W_m$, as for ZnO-Au or TiO_2-Au contacts discussed in detail in Section 6.3. When the two materials are brought into a contact, electrons start to flow from the semiconductor to the metal and vice versa. For the condition $W_{sc} < W_m$ more electrons will flow into the metal, and consequently the metal will become negatively charged. This process will continue until the system reaches the thermodynamic equilibrium, i.e. the Fermi energies are equal (Figure 9b), and the diffusion currents of the electrons flowing in both directions will be identical. The height of the potential barrier, which is formed at the interface of the two materials due to band bending, for electrons flowing from the semiconductor to the metal is defined by their work functions as $j = W_m - W_{sc}$. This potential difference is denoted as contact potential, and the barrier and the contact (for mentioned conditions) are known as Schottky barrier and Schottky contact, respectively.[127]

By means of e.g. X-ray or ultraviolet photoelectron spectroscopy (XPS or UPS), the work function and the distance of the valence band from the Fermi level can be determined. The band gap of the semiconductor is measured using ultraviolet-visible (UV-Vis) light spectroscopy. These three parameters provide information about the positions of E_c, E_F, and E_v versus the vacuum level. Examples of band alignment based on XPS and UV-Vis measurements for Au-TiO_2 and Au-ZnO are shown in Section 6.3.

2. Methods and sample preparation for characterization

In this chapter, the characterization methods are presented. The morphology, crystallinity and composition of the nanowires based structures were analysed using high resolution scanning electron microscopy (HRSEM), energy dispersive X-ray spectroscopy (EDX), X-ray diffraction (XRD), high resolution transmission electron microscopy (HRTEM) with high-angle annular dark-field imaging (HAADF), selective area electron diffraction (SAED), electron energy loss spectroscopy (EELS), and X-ray photoelectron spectroscopy (XPS). The general process and parameters used for the atomic layer deposition (ALD) and photoelectrochemical (PEC) measurements are described.

2. Sample preparation and characterization methods

2.1. High resolution scanning electron microscopy (HRSEM)

Scanning electron microscopy (SEM) is a widely used technique for characterization of the morphology of nanomaterials and nanostructures. It makes use of focused beam of accelerated electrons to scan the surface of the specimen and obtain a raster image. As an electron hits the surface of the sample, a number of interactions occur between the beam electrons and the atoms of the specimen resulting in emission of different types of electrons (secondary, backscattered, Auger) and rays (Bremsstrahlung, characteristic X-rays). By collecting the emitted secondary electrons on a cathode ray tube, topography image of the specimen is obtained. Collection of backscattered electrons emitted from deeper levels of the sample allows for contrast imaging of multicomponent structures when the atomic numbers of components differ widely

In this study, a high resolution scanning electron microscope (HRSEM, JEOL JSM-7401F) equipped with two secondary electron detectors at different positions with respect to the sample stage was used to image the fabricated membranes and nanostructures

Prior to the SEM analysis, the polymer membranes were sputter-coated with a ~8 nm thick Au layer (20 s) using an Edwards Sputter Coater S150B, by applying a pressure of 10^{-1} Torr and a potential of 1.5-1.6 kV resulting in a current varying between 15 and 20 mA. By the sputtered conductive layer the charging effects in SEM were avoided. The microscope was operated at an accelerating voltage of 4 kV in SEM mode. The topography and the pore size were analyzed with low secondary electron imaging (LEI) at a working distance of 8 mm.

To investigate the pore geometry inside polycarbonate membranes produced by heavy ion irradiation and subsequent chemical etching, the cross section of the membranes was imaged. The samples were prepared in collaboration with Dr. Loïc Burr (Materials Research department, GSI) by irradiating pre-etched membranes with high fluence of 5×10^{10} ions/cm^2 using Au ions with energy of 5.6 MeV/u followed by a 24 h UV treatment on each side of the samples. Due to the severe beam-induced embrittlement of the membranes easily break in liquid nitrogen which allows for imaging the cross section of the membranes. Alternatively, the embrittlement of the polycarbonate membranes was obtained by immersing the samples in Aqua Regia solution for ~2 month at room temperature. More details about this process can be found in the doctoral thesis of Dr. Loïc Burr.[128] After breaking the membranes, the samples were glued onto a specially designed SEM sample holder with a cut of 90° to section. Prior to the SEM analysis the samples were coated with ~8 nm Au, as described above. For these samples SEM was operated at 10 kV with LEI detector.

For SEM investigation of the nanowire arrays and networks, the polymer membranes were dissolved in dichloromethane (CH_2Cl_2 for analysis, Merck) in several steps. The nanowire arrays/networks embedded in the polymer membranes were placed horizontally in sample

holders in such a way, that the edges were fixed to avoid bending of the sample which can cause damage to the wires. CH_2Cl_2 was dropped continuously on top of the sample until the level of dichloromethane (with polymer residues) reached the sample holder but did not cover the sample. If the solution covers the sample, it might contaminate the surface of the sample with the dissolved polymer residues. A continuous flow of CH_2Cl_2 was found to be an important step. If the sample with partially dissolved polymer was exposed to air for a relatively long time (a minute or more), it seemed to harden resulting in broken the wires. After repeating this step twice, the samples were immersed in fresh CH_2Cl_2 bath and left for 1h. This latter step was repeated three to four times. Finally, the free-standing nanowire arrays and 3D nanowire networks with the metallic electrode were dried in air and inspected by SEM. Both ZnO and ZnO/TiO_2 nanowire arrays, networks and films were characterized by using SEM in gentle beam low mode (GB-Low) with an upper secondary electron detector imaging (SEI) at 2 kV accelerating voltage at a distance of 6 or 8 mm.

For nanowire diameter and length analysis, single nanowires were transferred onto Si wafers pre-cleaned with acetone and deionized water. The following two methods were applied: (i) after dissolution of the membrane, some of the wires were detached from the back electrode by exposing the sample is immersed in CH_2Cl_2 to an ultrasonic bath (Elma, Transsonic T460/H) for a few seconds. The released nanowires were then transferred onto a Si wafers by drop-casting the nanowire/CH_2Cl_2 mixture. (ii) The wires still embedded in the membrane were immersed in dichloromethane in centrifuge tube. After an ultrasonic treatment for 15-20 s, the tube was centrifuged three to five times at 4000 rpm for 20-30 min using Heraeus Biofuge primo R Centrifuge. In between these steps, the dichloromethane bath was replaced with a fresh one. Before each step of centrifugation, the nanowires with the fresh dichloromethane were mixed on a shaker for 2 min to disperse the wires in the solution for better cleaning. Finally, the solution containing the wires was drop-casted onto Si wafers. The samples were analyzed by operating the SEM at the same conditions as for nanowire arrays and networks attached to their substrates.

Core-shell nanowires and small pieces of nanowire networks were transferred onto Au-TEM grids (Plano GmbH) by drop-casting the wires with CH_2Cl_2 onto the grid. To analyze the samples in transmission mode by SEM, 10 kV accelerating voltage was applied and the wires were imaged with LEI detector at a working distance of 8 mm. To study the dispersity of the nanowires, which were transferred onto TEM grid by bobing the grid on the surface of the network, GB-Low mode at 2 kV and probe current of 7 at a distance of 8 mm was used.

2.2. Energy dispersive X-ray spectroscopy (EDX)

Characteristic X-rays emitted from the sample depend on the atomic number of elements in the structure and are mainly used for quantitative and qualitative chemical analysis

The composition of the nanowire arrays, networks and single wires was studied by energy dispersive X-ray spectroscopy (Bruker) in the SEM. Multipoint spectra and line scans were recorded by applying an accelerating voltage of 10 or 20 kV and a probe current of 10 depending on the amount of material present, at a fixed distance of 8 mm. The acquisition time was ~8 min for multipoint scans and ~10 min for line scans. The analysis of the spectra was done by using the Quantax software from Bruker.

2.3. X-ray diffraction (XRD)

XRD is a nondestructive technique that uses collimated beam of X-rays to investigate the arrangement of atoms within a crystal. When an X-ray beam strikes the sample it diffracts in different directions from the atoms of crystal planes. If the wavelength of the X-rays, λ, the incident radiation angle, θ, and the crystal lattice d-spacing satisfy Bragg's law ($n\lambda = 2d\sin\theta$), constructive interference is produced and the diffracted X-rays can be detected. The recorded diffractogram provides information about crystal phase, crystallographic orientation and lattice parameters of the crystal, defects, stresses, etc.

The crystallographic structure of the cylindrical and conical nanowire arrays still embedded in the membrane was analyzed by using an X-ray diffractometer (XRD, Seifert X-Ray generator, HZG-4 goniometer in Bragg-Brentano geometry) with a generator voltage of 40 kV and a current of 30 mA using Cu Kα radiation (λ = 1.54056 Å). The device was operated by the Rayflex software. The scan rate and integration time were respectively.

The XRD patterns of networks after dissolution of the membrane were recorded with a D2 PHASER diffractometer (Bruker), which was operated at a generator voltage of 30 kV and current of 10 mA (Cu Kα radiation). With this device the scan rate and integration time were 0.05° and 20 s, respectively, and the measur™ software.

2.4. High resolution transmission electron microscopy (HRTEM)

Transmission electron microscopy (TEM) is one of the techniques allowing for analysis of material structure on an atomic scale. It enables the analysis of the crystal structure, chemical composition and contaminations through diffraction pattern, X-ray and electron energy loss analysis. In TEM accelerated electrons are projected onto a thin specimen and penetrate the sample undergoing either elastic or inelastic scattering with its atoms. The transmitted and elastically scattered electrons are used to build a high resolution TEM image and/or record selected area electron diffraction (SAED) pattern. Inelastically scattered electrons that lose energy are detected by a high-angle annular dark-field (HAADF) detector for mass contrast imaging and/or by a spectrometer for electron energy-loss spectroscopy (EELS) allowing for chemical mapping and composition profile analysis.

To analyze the crystallinity and purity of ZnO and ZnO/TiO_2 wires, as well as the homogeneity and phase of TiO_2 layers coated on top of ZnO wires by atomic layer deposition

(ALD), the wires from arrays and networks were transferred onto a TEM grid as explained in Appendix E. In collaboration with Dr. Wilfried Sigle from the MPI for Solid State Research in Stuttgart the wires were inspected by using high resolution transmission electron microscope (HRTEM, JEOL ARM200CF) together with high angle annular dark field (HAADF) imaging and electron energy loss spectroscopy. Selected area electron diffraction was used for analysis of the crystallographic structure of the wires in micro-scale. The device was operated at an accelerating voltage of 200 kV and an emission current of 15 µA.

2.5. Photoelectrochemical (PEC) measurements

The photoelectrochemical (PEC) measurements presented in the thesis were performed at the GSI in Darmstadt and Univeristy of Twente (The Netherlands) in the group of Prof. Dr. Guido Mul.

The setup at the GSI consisted of a LS0108 solar simulator from LOT Quantum Design GmbH (AM 1.5G), a Reference 600™ potentiostat (GAMRY Instruments) and a PECC-2 photoelectrochemical cell (ZAHNER-Elektrik GmbH & Co. KG) with a 8 mm O-ring defining the photoactive area of the sample.

For the PEC measurements at the University of Twente a setup consisting of a 300 W Xe lamp with AM 1.5 filter (Newport corporation), a potentiostat (VERSASTAT4, Pinceton applied reserach), and PEC-2C photoelectrochemical cell (ZAHNER-Elektrik GmbH & Co. KG) with a 7 mm O-ring were used

All measurements were performed in 0.1 M K_2SO_4 (Sigma Aldrich) aqueous solution with a pH of 5.6. The distance of the PEC cell was calibrated with a Si solar cell (Newport Oriel, P/N 91150V) to obtain an illumination of 1 sun on the sample.

2.6. X-ray photoelectron spectroscopy (XPS)

X-ray photoelectron spectroscopy (XPS) is a surface sensitive technique employed for analysis of chemical composition and electronic states of a material within a depth of ~10 nm on the surface of a specimen. When an incident photon (X-ray) hits the surface of the sample with energy higher than the ionization energy of the material, electrons are ejected from the samples. The kinetic energy E_{kin} of the released electrons can be detected by a photoelectron spectrometer. It related to incident photon energy $h\nu$ by $E_{kin}=h\nu-(E_b+F_s)$, where E_b is the binding energy required to transfer the excited electron to the Fermi level, F_s is the work function of the spectrometer. A spectrum revealing the number of ejected electrons versus kinetic energy provides information about the energy levels in the inner electron shells of the specimen atoms.

XPS was applied to analyze the surface of nanowire networks to identify modifications and/or corrosion of the surface after PEC measurements as well as to estimate possible contaminations on the wires (e.g. residues from polymer or dichloromethane) which might

affect the PEC performance. XPS was also used to determine the work function and the valence band positions for visualization of the band alignment of ZnO and Au-TiO_2 Schottky contacts. The measurements were performed at the DArmstadt Integrated SYstem for FUNdamental research) of the Surface Science group of Prof. Dr. Wolfram Jaegermann at the TU Darmstadt in collaboration with Dr. Florent Yang. The spectra were recorded by using a PHOIBOS 225 (Specs GmbH) analyzer and a monochromatic Al KŬ radiation with excitati measurement, the system was calibrated with a high purity Ag sample (freshly sputter cleaned under Ar atmosphere) with a very high purity to calibrate the Fermi level. For determination of the work function, a negative bias of 3 V was applied between the analyzer and the sample for distinguishing the signal from the sample.

3. Fabrication of etched ion-track membranes

Ion irradiation and etching processes required for the fabrication of etched ion-track polymer membranes are described in this chapter. Three main geometries are discussed: vertically aligned cylindrical and conical channels as well as interconnected channel networks. Superstructures consisting of both vertically aligned and interconnected channels are introduced.

3. Fabrication of etched ion-track membranes

Etched ion track membranes were prepared by chemical etching of ion irradiated foils. During this process the damaged material in the tracks is selectively removed converting the ion tracks into channels (pores). By adjusting the ion fluence (number of ions per area) the number of pores in the membrane can be controlled since each ion passing through the polymer foils creates one track. Using different irradiation and etching conditions (e.g. concentration of the etchant, temperature, and etching time and setup configuration), polycarbonate membranes were fabricated with parallel cylindrical, parallel conical and interconnected cylindrical nanochannels (Figure 10). Irradiation and etching conditions employed for the fabrication of these three types of templates are presented in the following section.

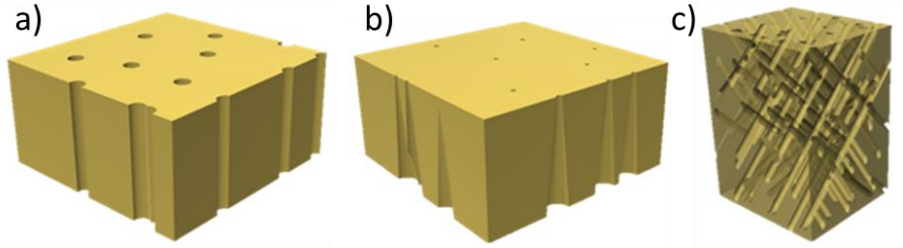

Figure 10. Schematic representations of membranes with a) parallel cylindrical, b) conical and interconnected cylindrical pores.

3.1. Parallel cylindrical pores by symmetric etching

Polycarbonate (PC) foils with a thickness of 30 µm (Makrofol N, Bayer AG) were irradiated with ~2 GeV Au and Bi ions at the X0-beamline of the universal linear accelerator (UNILAC) at GSI. In order to fabricate membranes with parallel nanochannels, the irradiation was performed under normal beam incidence (perpendicular to the foil surface), typically applying a fluence of 10^9 ions/cm^2. Prior to etching, both sides of the irradiated polymer foils were exposed to UV light (30 W, 312 nm, T-30M, Vilber Lourmat) in air to improve the homogeneity of the pore diameter distribution over the whole sample.[81,129] By immersing the irradiated foils in a 6 M sodium hydroxide (NaOH, Sigma Aldrich, > 97 %) solution at 50 °C, the tracks were selectively dissolved and converted into cylindrical channels. Given by the general etching of the bulk polymer the total thickness of the membrane slightly decreases (Figure 11a).[76] Symmetric etching was performed in a double-walled cylindrical pot connected to a heating water circuit (Figure 11b). In this configuration the etching solution had an access to the tracks from both sides of the irradiated foils. In order to improve the convection and to keep the bath temperature constant, the etching solution was stirred at ~250 rpm. To produce multiple membranes with identical pore diameter, four samples were etched at the same time. Various etching times were employed between 1.5 and 8 min. The schematic of the evaluation of the track etch and the channel opening with the increase of time are shown in Figure 11c. Under these etching conditions, the pore diameter increased linearly with etching time. However, the etching rate varied depending on the aging of the

polymers, i.e. the time period between irradiation and etching processes. Longer aging periods led always to higher etching rates. The values usually varied between 20 and 30 nm/min. After etching, the membranes were rinsed with deionized (DI) water by immersion in multiple water baths, and finally dried in air.

Figure 11: Schematic representations of a) etching of a single. Nanochannel formation requires a high track etch rate compared to the bulk etch rate, b) thermostated pot for symmetric etching, c) the nanochannel opening process for different etching times

Pore size and size distribution were analyzed by HRSEM. For membranes etched without UV treatment an inhomogeneous size distribution of the pores was observed (Figure 12a). The areas marked with red and orange circles in Figure 11a show smaller and larger pores with average diameters of 170.22 and 350.74 nm, respectively, as compared to the mean diameter of the majority of the pores being 307.9 nm. A pre-sensitization step with 1h UV light on each side of the irradiated foils before etching yielded a more homogeneous etching and size distribution (Figure 12b). The average pore diameter of this sample was 291.20 nm.

Figure 12: Representative SEM images of the surface of track-etched membranes etched under identical conditions a) without and b) with UV pre-treatment showing a broad (a) and uniform (b) distribution of the pore diameters.